Heterocellular and homocellular electrically coupled networks of the thalamus and cortex revealed by focal photomapping

Abbreviated title: Opto-δL maps coupled networks

Authors: Mitchell J. Vaughn[1], Kevin J. Bender[2] and Julie S. Haas[1*]

Affiliations:

1. Department of Biological Sciences, Lehigh University, 111 Research Drive, Bethlehem, PA 18015 USA

2. Weill Institute for Neurosciences and Department of Neurology, University of California, San Francisco, San Francisco, CA, USA

Author Contributions: JSH and KJB designed the method and experiments. MJV optimized the method and performed the electrophysiological research. MJV and JSH wrote and revised the manuscript. JSH supervised and acquired funding.

Correspondence: Julie S. Haas, juliehaas@lehigh.edu

Number of figures: 4 figures

Number of tables: 0 tables

Number of multimedia: 0 multimedia

Number of words for abstract: 179 words

Number of words for Introduction: 621 words

Number of words for Discussion: 816 words

Acknowledgements: We thank all members of the Haas and Bender laboratories for input and discussion.

Conflict of interest: The authors report no conflict of interest

Funding: NIH R01 NS128713, Whitehall Grant in Aid to JSH

Abstract

Electrical synapses are present widely across the mammalian brain and are crucial components of active neural circuitry and connectomes. Identification of electrically coupled networks in living tissue has been limited by technical demands of multiplexed recordings, and no dyes, fluorescent reporters, or genetic labels are currently able to fill the gap. Here, we introduce a novel method of identifying and measuring electrical synapses: opto-δL combines focal photostimulation of soma-targeted opsins and a novel method for computing the strength of electrical synapses, based on spike timing, to rapidly measure and map electrically coupled networks *in vitro*. We measured electrical synapses and characterized coupled networks in mature thalamic reticular nucleus (TRN) and in cortex. We used opto-δL to show that TRN neurons form functional networks that extend as far as 100 μm, and that TRN neurons synapse promiscuously, coupling both matching and disparate genetic subtypes of neurons. Future applications of opto-δL will allow identification and characterization of coupled networks across the brain and enable circuit and systems-level interrogations of the identity and roles of electrical synapses in circuitry, behavior, and cognition.

Introduction

Chemical and electrical synapses, the twins of the foundational Golgi-Cajal debate, together compose the basis of interneuronal communication across the brain. Neurotransmitter-based chemical synapses underlie communication that is primarily unidirectional and stereotyped in timecourses of activation and decay. In contrast, electrical synapses formed by gap junctions (GJs) relay neuronal signals of any size, polarity, and timecourse bidirectionally between coupled cells, and they do so without the requirement or cost of a spike for signal transduction. Most mature mammalian GJs comprise paired hexameric channels of connexin36[1-3] , which is expressed widely in GABAergic neurons throughout the brain[4]. While chemical synapses and the neuronal networks they form have been described in exquisite detail, descriptions of electrical synaptic transmission and, importantly, their functional networks have been much more limited.

Electrical synapses are increasingly appreciated for the diverse roles they play throughout the brain. They are most widely characterized as mediating synchronization of oscillatory activity in neuronal circuits[5-15]. Beyond synchronization, electrical synapses directly mediate feedforward and lateral excitation, inhibition, reduce signal to noise ratio, sharpen coincidence detection, and facilitate object discrimination[16-32]. GJs create uniquely offset receptive fields in retinal ganglion cells, where they also contribute to tuning responses, enhanced signal saliency, sensitivity, and enhanced coding of visual features[16, 33-36].

Our understanding of the roles electrical synapses and networks play within neuronal networks is sharply limited by the tools currently available. The gold standard for measuring electrical synapses is through paired recordings, in which current is injected into one neuron and a hyperpolarizing deflection can be measured in a coupled neuron[37]; the ratio of deflections indicates synapse strength. While this method is the most direct, it is time-intensive, low-

70 throughput, and limited to single synapses *in vitro*. Only one experiment has successfully
71 recorded from a small sample of coupled neurons *in vivo*[38]. Dye-coupling methods[39-46] confound
72 primary, secondary, or tertiary connections, fail to quantify the strength of synapses, and have
73 been limited to fixed tissue, although modern variations of dye-coupling have used exogenously
74 applied molecules that diffuse across a GJ, rendered more specific by limiting entry[47] or
75 fluorescence[48] to genetically labeled cells. For these reasons, electrical synapses and networks
76 remain neglected relative to their chemical counterparts in our modern understanding of the
77 brain.

78 The thalamic reticular nucleus (TRN) is a nucleus of GABAergic neurons[49] that provide the
79 majority of inhibition to sensory thalamic relay areas and are hypothesized to focus the
80 searchlight of attention to the sensory surround[50]. TRN is composed of distinct neuronal subtypes
81 with spatially and genetically distinct expression[51-53], and our previous paired recordings
82 indicated that homocellular and heterocellular electrical synapses (coupling same and disparate
83 cell subtypes) of the TRN[54] may provide the only thalamic link between distinct but parallel
84 thalamocortical relay channels[51-53, 55]. Because visualization of TRN neurons is impeded by
85 myelination of thalamocortical fibers after eye opening, all paired-patch experiments
86 characterizing electrical synapses in TRN have been limited to juveniles[12, 54, 56-62]. While
87 connexin36 (Cx36) expression persists into adulthood[63] and spikelets have been reported in
88 adults[64], the possibility that the contributions of GJ networks to thalamocortical relay are limited
89 to developmental stages remains.

90 Here, we leverage focal photostimulation of soma-targeted opsins to detect and measure
91 electrical synapses via changes in spike timing and to map electrically coupled networks in adult
92 thalamic reticular nucleus (TRN). [49-54, 63, 64] and cortex. Our maps of electrically coupled

networks in adult TRN demonstrate that coupled networks comprise both heterocellular and homocellular electrical synapses that range from 1 to 4 synapses in size and extend as far as 100 μm of distance. In addition to providing a new and efficient toolset for measuring and mapping electrical synapses and networks across the living brain, our results provide insight into the neural circuits that underlie attentional focus on the sensory surround.

Results

Precision of neuronal spike timing is a tightly controlled fundamental process[65] that is crucial for fidelity of information processing, and is often a parameter of interest in neural coding[66-70]. Electrical synapses are important contributors in determining spike times[30, 31, 58]; activity in a coupled neighbor can shift spike times of a neuron responding by tens of ms[58]. Leveraging this powerful effect of electrical synapses, we previously compared spike timing differences due to electrical synapses in two cases using paired recordings: 1) rheobase stimulation in one neuron alone (t_1) and 2) rheobase stimulation with simultaneous activation of a coupled neighboring neuron (t_2). We calculated the percentage change in latency of evoked spikes, δL, as:

$$\delta L = \frac{100 * (t_1 - t_2)}{t_1}$$

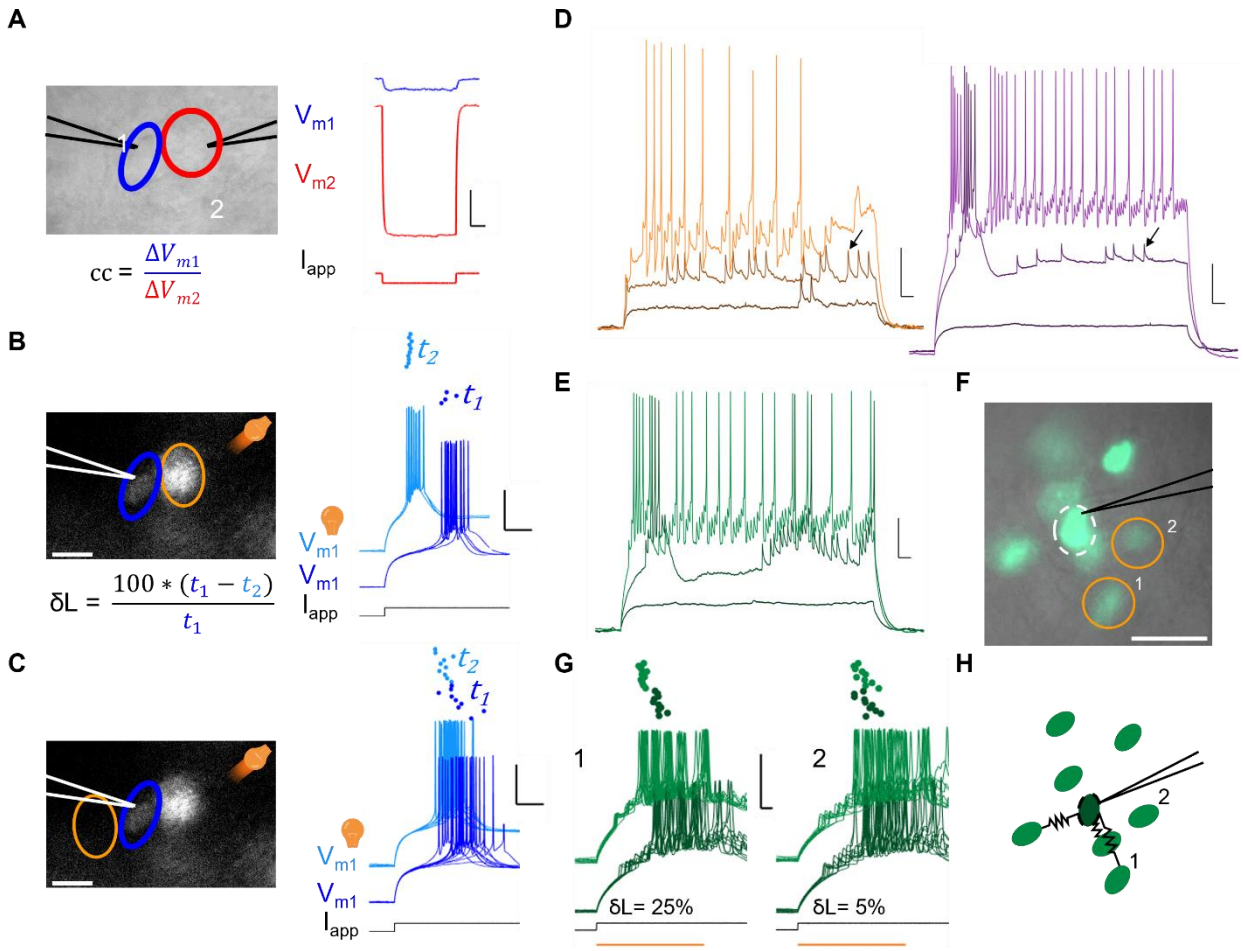

Figure 1: **Electrical coupling measured by paired patching and opto-δL in the same pair**.
A. IR image of a patched pair of TRN juvenile neurons (red and blue circles). Right: voltage responses (V_m) from both neurons during current injection (I_{app}) into cell 2. The coupling coefficient (cc) is the ratio of voltage deflections in both cells; cc = 0.08. Scale bars 100 ms, 2 mV.
B. Left: Live fluorescence image of the same pair showing st-ChroME-mRuby expression in both neurons. Orange circle indicates area of focal photostimulation of cell 2. Scale bar: 12.5 µm Right: Spiking in neuron 1 for 100 pA applied current (dark blue) alone, and with simultaneous focal photostimulation of neuron 2 (light blue). Dots mark the time of the first spike in each interleaved trial. δL was calculated from the difference in mean spike latencies with (t_2) and without (t_1) photostimulation; δL = 43.4%;
C. Left: Same image as in B. Orange oval marks the area of focal photostimulation of a blank spot that is equidistant from neuron 1. Right: Spiking in neuron 1 for 110 pA applied current alone (dark blue), and with simultaneous photostimulation of the blank spot (lighter blue) from interleaved trials. Dots mark the time of the first spike in each trial. Scale bars 50 ms, 20 mV. For the blank spot used in trial **C**, δL = 16.3%. Differences between δL for trials in **B** and **C** were significant ($p < 0.01$, Wilcoxon signed-rank test).
D. In two separately patched neurons from adult tissue, increasing amplitudes of current injection into the cell revealed spikelets (arrows) driven by shared excitation of an unrecorded coupled neuron. Scale bars: 25 ms, 10 mV. **E.** Spikelets in a third patched neuron.
F. IR image of the patched neuron from **E** with fluorescence overlay from two depths.
G. Two opto-δL measurements in the patched cells during photostimulation of the cells circled and numbered in **F**. Darker traces are responses from photostimulation of equidistant control locations, and light green traces are from photstimulation of the corresponding numbered cell in **G**. We identified that the cell labeled 1 was one of two powerful synapses (δL = 25%) generating the spikelets in **E**.
H. Diagram of the coupled network embedded within all tested neurons from **F**. Scale bar: 25 µm.

This quantity is well-correlated with traditional measures of the strength of electrical

synapses[71]. Here, we combined measurements of δL with focal photostimulation of a soma-targeted opsin, st-ChroME[72], in potentially coupled nearby neurons, thereby reducing the requirement for recording an electrical synapse to one patched neuron and simultaneously widely expanding the number of potential synapses tested. We refer to this method as opto-δL.

To map electrically coupled networks using opto-δL we injected AAV9-CAG-DIO-ChroME-st-P2A-H2B-mRuby into the TRN of PV-Cre or SOM-Cre mice, and after at least two weeks, prepared acute brain slices from those mice. We first validated opto-δL in a patched pair of neurons, with both neurons expressing st-ChroME, in juvenile tissue. We measured the coupling coefficient for the synapse between these neurons using the traditional small hyperpolarizing current injections to one of the neurons (Fig. 1A); the coupling coefficient (cc) is the ratio of voltage deflections in both neurons in response to current injection into one. This pair had a mean cc of 0.075, close to the average value for coupling between pairs of TRN neurons[73]. Next, we used a digital mirror device (Polygon) to deliver 1-photon focal (34 - 50 μm^2) 560 nm photostimulation to nearby regions of interest, including the neighboring neuron, during trials of rheobase-drive spiking in the patched neuron, and computed δL. For all targeted regions of interest, we used a light intensity sufficient to drive spiking when focused directly on the soma of a patched neuron (see Methods; Supp. Fig. 1). Because both 1-photon and 2-photon photostimulation result in light scattering in live tissue[74-76], we measured spike times in cell 1 when photostimulating a blank spot that was equally distanced from cell 1 as the neighboring neuron (cell 2) as a control for any light scattering-induced excitation of cell 1. Driven by rheobase current (100 pA) alone, cell 1 spiked 176 ± 3 ms after stimulus onset (Fig. 1B, dark blue traces). In interleaved trials, we applied rheobase stimulation to cell 1 and focal photoexcitation of the neighboring neuron; for those trials, cell 1 spiked with a latency of 99 ±

133 0.3 ms. (Fig. 1B, lighter blue traces), and we computed δL for the synapse: δL = 43.4%. To
134 compared δL f or cell 2 to δL driven by scatter excitation to a blank spot, we applied concurrent
135 photostimulation of the blank spot and injection of rheobase current to cell 1, which resulted in
136 spikes with latency of 148 ± 3 ms (Fig. 1C, light blue traces) and produced δL of 16.3%. δL was
137 significantly larger (by 27.1%; $p < 0.01$, Wilcoxon signed-rank test) for photostimulation of the
138 neighboring cell 2 compared to the blank spot, allowing us to conclude based on spike latencies
139 that the neighboring cell 2 was coupled to the patched cell 1. These measurements validate the
140 use of a single electrode and focal optogenetics to identify and characterize an electrical synapse
141 and provide a foundation for its application to studying electrical synapses and networks in
142 heavily myelinated adult TRN tissue that precludes paired patching but where spikelets provide
143 evidence of electrical synapses (Fig. 1D). Indeed, observations of spikelets in adult tissue pointed
144 us towards identification of electrically coupled neighbors through δL (Fig. 1E-H).

145 Genetically and anatomically distinct sets of neurons form distinct sets of relay pathways
146 through the thalamocortical system[51-53, 55]; electrical synapses in the TRN may be the only
147 thalamic link between these information channels. We previously used paired recordings in
148 juveniles to test whether TRN electrical synapses interconnect neurons of distinct cell types[54].
149 Those experiments necessitated the use of crossed Cre reporter mice to label neurons for juvenile
150 recordings, presenting an additional possible confound of mislabeling neurons due to Cre off-
151 target recombination [77]. To identify, measure and characterize homocellular and heterocellular
152 electrically coupled networks in adult TRN, we injected Cre-dependent st-ChroME into adult
153 mice to genetically identify subsets of neurons (Fig. 2). To map homocellular electrical synapses,
154 we patched ChroME-expressing mRuby+ neurons in SOM-Cre mice (SOM+), and measured δL
155 induced by focally photostimulating other nearby mRuby+ neurons (Fig. 2A). To map

156 heterocellular electrical synapses, we patched mRuby- neurons in SOM-Cre mice (SOM-), and

157 measured δL induced by focally photostimulating nearby mRuby+ neurons (Fig. 2B). We also

158 measured homocellular

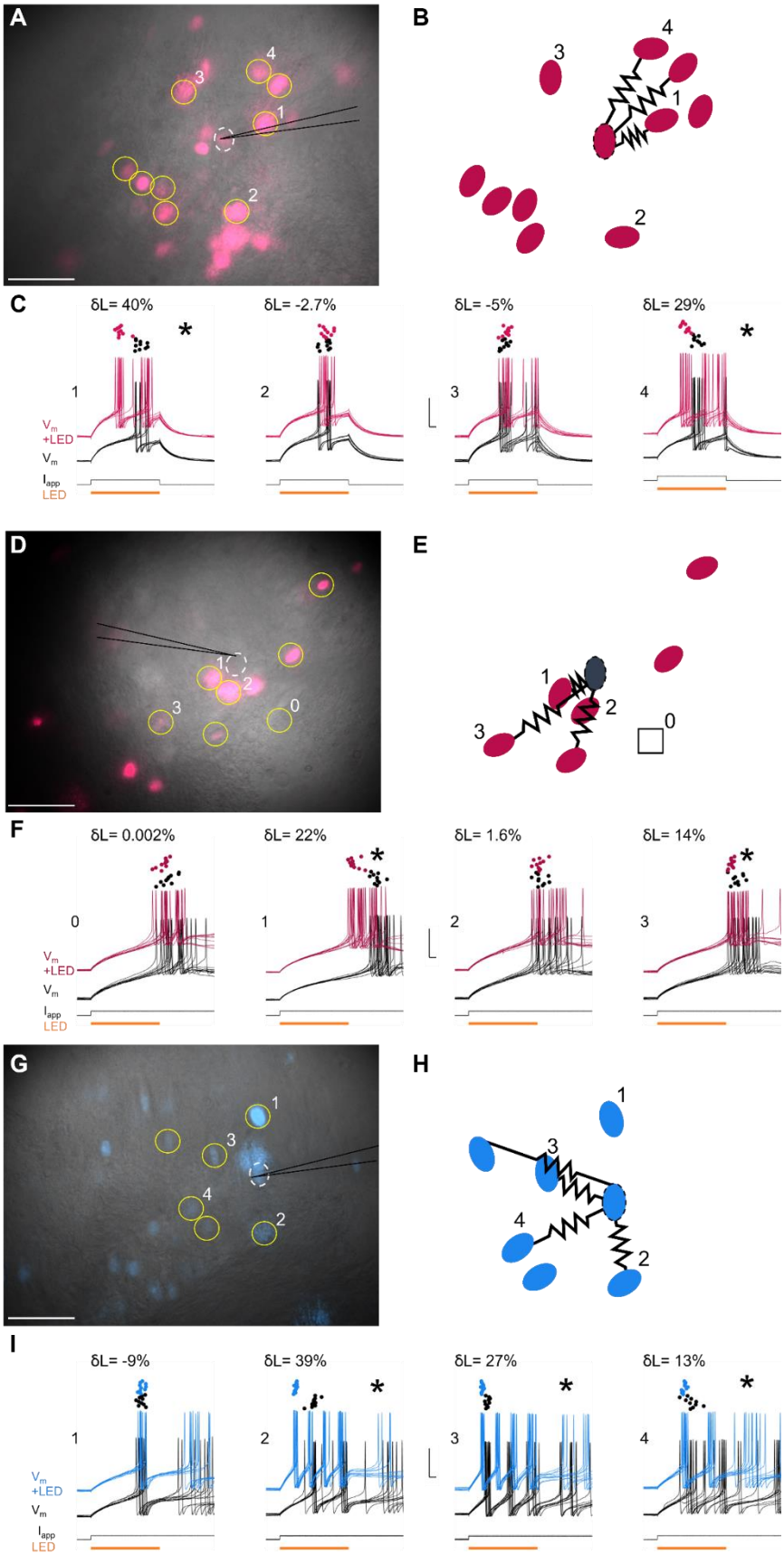
A
B
C
δL= 40%
δL= -2.7%
δL= -5%
δL= 29%
Vm +LED
Vm
Iapp
LED
D
E
F
δL= 0.002%
δL= 22%
δL= 1.6%
δL= 14%
G
H
I
δL= -9%
δL= 39%
δL= 27%
δL= 13%

Figure 2: **Maps of coupled networks between TRN neurons**.
A. Representative homocellular network amongst SOM+ neurons. Overlay of IR and fluorescence images from live recording of st-ChroME-mRuby-expressing neurons in SOM-Cre mouse. Fluorescence is pseudocolored magenta. The patched neuron is circled with white dashes. Scale bar: 50 µm.
B. Diagram of the coupled network embedded within all tested neurons from **A**.
C. Spiking responses used to measure δL and identify network in **A**. Dots mark the times of first spikes in the patched neuron from each trial. Black traces are responses of the patched neuron during rheobase-only trials and colored traces are responses during added target cell photostimulation. Traces are vertically offset for clarity. Each set of traces is numbered by the corresponding cell in A. Scale bars: 5 ms, 20 mV. p values (Wilcoxon signed-rank test) for δLs: 1) < 0.01, 2) 0.70 3) 0.34, 4) < 0.01.
D - F: Representative heterocellular network between SOM- and SOM+ neurons., as described for **A-C.** p values (Wilcoxon signed-rank test) for δL: 0) 1.0, 1) < 0.01 2) 0.56, 3) < 0.01.
G – I: Example homocellular network between PV+ neurons, as described for **A-C**. p values (Wilcoxon signed-rank test) for δL: 1) 0.98, 2) < 0.01 3) <0.01, 4) 0.03.

networks in PV+ neurons (Fig. 2C). To compensate for excitation from scatter in these experiments, we developed correction procedures for each recorded neuron (Supp. Fig. 3; see Methods); scatter effects depend on factors including light intensity, opsin expression, and input resistance, as well as distance but diminished to insignificant levels by 50 - 100 µm (Supp. Fig. 2). We note that mapping heterocellular networks has the advantage of targeting opsin-lacking neurons for recording, thereby averting the need for compensation in those experiments.

We implemented opto-δL in a population of n = 398 cells comprising 64 possible coupled networks. Overall, we measured values of δL that were significantly different from 0 within all combinations of genetic subtypes tested (Fig. 3A). We measured significant values of δL between SOM+ and other SOM+ neurons in 16 of 35 possible homocellular SOM networks. The mean coupling rate was 15.1% across all tested connections (n = 206 possible connections), and 40.3% across all tested connections within networks that contained at least one electrical synapse (n = 67 possible connections). The mean δL between SOM+ neurons was 25.0 ± 3.2%, and the mean homocellular SOM network contained 1.7 ± 0.1 direct electrical synapses (Fig. 3B). Between SOM+ and SOM- neurons (Fig. 3C) we measured significant values of δL in 4 of 12 possible heterocellular networks. The mean coupling rate was 7.3% across all tested connections (n = 85 possible synapses) and 25.8% across all tested connections within networks that

contained at least one electrical synapse (n = 31 possible synapses). The mean δL for SOM+ to SOM- connections was 16.4 ± 2.4%, and the mean heterocellular network contained was 2.0 ± 0.2 direct electrical synapses (Fig. 3C). For connections between PV+ and PV+ neurons, we measured significant values of δL in 13 of 17 homocellular networks. The mean coupling rate was 25.9% across all tested connections (n = 108 possible synapses), and 39.1% across all tested connections within networks that contained at least one electrical synapse (n = 74 connections). The mean δL for PV+ to PV+ electrical synapses was 18.9 ± 2.8% (Fig. 3D), and the mean network size was 2.2 ± 0.1 direct electrical synapses (Fig. 3D). Across networks, there were no significant differences in δL between subtypes (Fig. 3B-3D, $p > 0.05$). The mean δL across all subtypes was 22.8% ± 1.9% (n = 67 synapses), and 50% of synapses had a δL between 11.0% and 33.3%. The largest δL was 68.4%. We observed several instances in which no nearby opsin-expressing neuron had any electrical synapses to the recorded neuron. It was rarer for there to be no electrical synapses between PV neurons (Fig. 3B-D, $p < 0.01$, chi-squared test). PV neurons had no electrical synapses to nearby opsin-expressing cells in 23.5% of recorded neurons, while SOM+ neurons had no connections 54.3% of the time, and SOM- neurons had no connections 66.7% of the time. There was no difference between SOM+ and SOM- neurons in the frequency of cells that had no nearby electrical synapses ($p = 0.07$, chi-squared test).

Measuring electrical synapses by patching pairs introduces spatial selection biases to the pairs that are ultimately tested in experiments; this effect may have contributed to discrepancy between results from rat TRN suggesting that electrical synapses occur within intersomatic distances less than 40 μm[73], while dye-coupling results indicate a median intersomatic distance of 80-120 μm[62]. We used opto-δL to more exhaustively sample the spatial extent of coupling for distances up to 250 μm. In our data, across all neuron types grouped together, we confirmed that

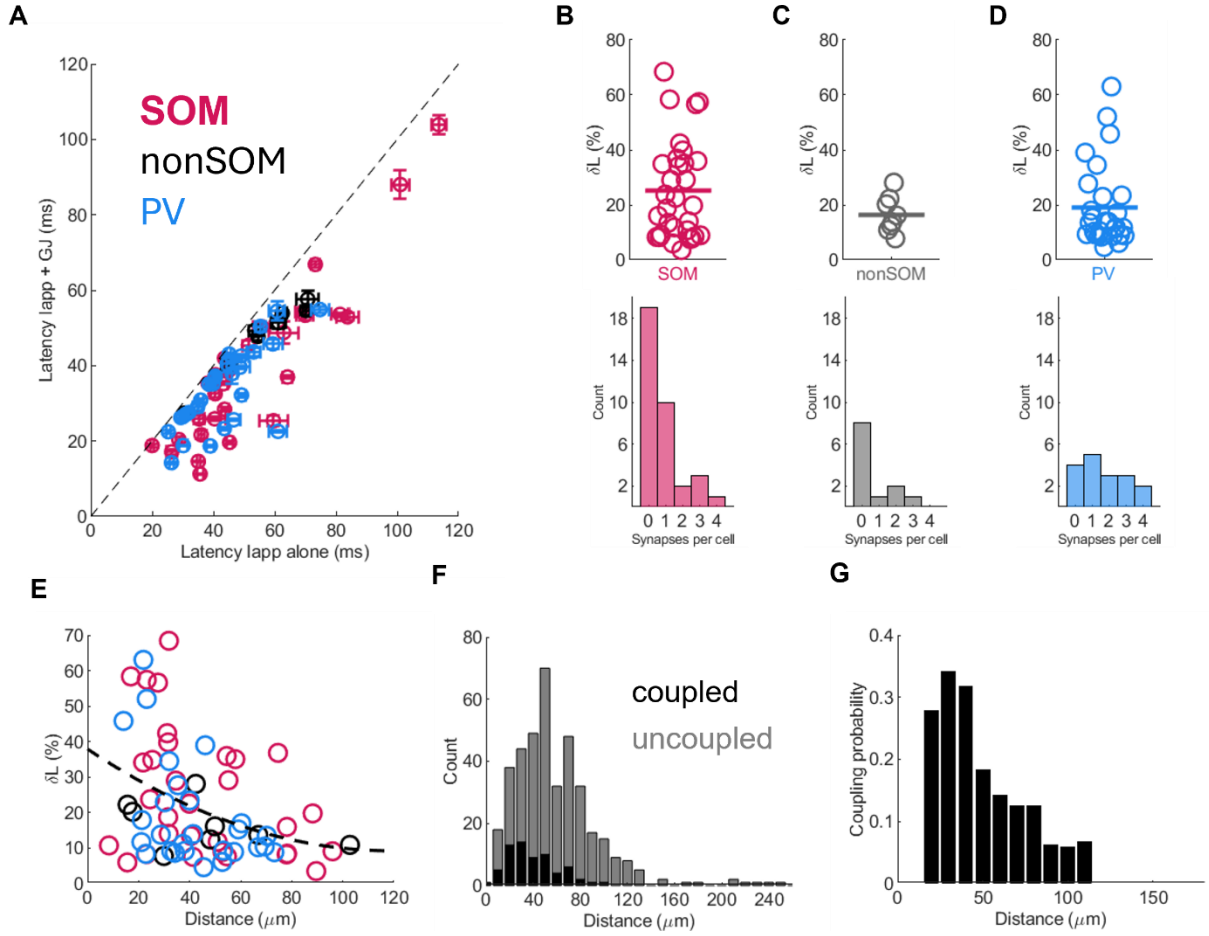

Figure 3: Distributions of electrical synapses over strength and space for TRN networks.
A. Latencies (+/- SEM) used to compute δL for all δL values determined to be significant.
B. Top: δL for homocellular SOM+ synapses (mean δL = 25.0 ± 3.2%, n = 31 synapses). Bottom: network sizes for SOM+/SOM+ networks (mean size: 1.7 ± 0.1 synapses per map).
C. As in **B,** for heterocellular SOM-/SOM+ synapses (mean δL = 16.4 ± 2.4%, n = 8 synapses; mean size 2.0 ± 0.2 synapses per network).
D. As in **B** for PV+/PV+ synapses (mean δL = 18.9 ± 2.8%, n = 28 synapses; mean size 2.2 ± 0.1 synapses per network, n = 13 maps).
E. Distribution of δL across intersomatic distance for each subtype in TRN (n = 67 synapses). Fit: single exponent.
F. Number of photostimulated neurons that were (black) or were not (grey) coupled to a patched neuron, plotted against distance from the patched neuron (n = 398 neurons).
G. Probability of coupling versus intersomatic distance (n = 398 neurons).

TRN neurons that were closer together were stronger (Fig. 3E) and more likely to be coupled (Fig. 3F-G), confirming previous reports that δL decreases with intersomatic distance. Collectively, our data showed that electrically coupled networks for all cell types link neurons as far as 100 µm apart (Fig. 3F).

To establish whether opto-δL is a viable tool for mapping coupled networks across the brain, we used opto-δL to identify and map coupled networks in somatosensory cortex using st-

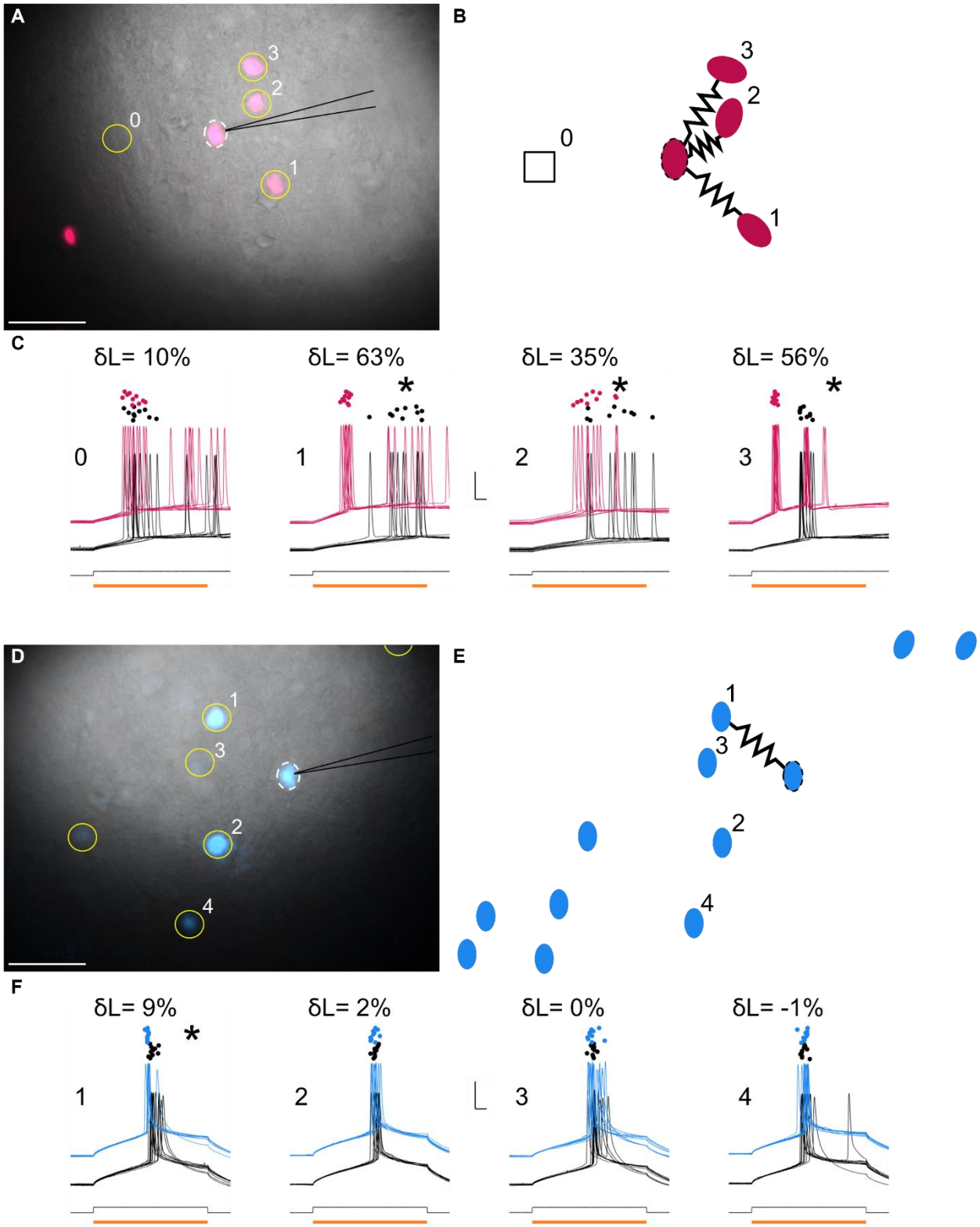

ChroME-mRuby expression to identify possible members of the network. In a SOM-Cre mouse (Fig. 4A), we identified one network that comprised four neurons, with average δL of 51.4% and

Figure 4: Maps of coupled networks between cortical GABAergic neurons.
A. Network between SOM+ cortical neurons. A) Overlay of IR and fluorescence images of st-ChroME-mRuby-expressing neurons in SOM-Cre mouse. Fluorescence is pseudocolored magenta. The patched neuron is circled with white dashes. Scale bar 50 µm.
B. Diagram of the coupled network embedded within all tested neurons from A.
C. Spiking responses used to measure δL and identify network in A. Dots mark the times of first spikes in the patched neuron from each trial. Black traces are responses during control trials (Iapp only) and colored traces are responses during target cell photostimulation. Traces are vertically offset for clarity. Each set of traces is numbered by the corresponding cell in A. Scalebars are 5 ms, 20 mV. p values (Wilcoxon signed-rank test) for δL: 0) 0.13, 1) < 0.01 2) 0.01, 3) 0.01.
D – F: Example network between PV+ neurons, as described for **A - C**. p values (Wilcoxon signed-rank test)

average intersomatic distance of 43.8 µm. In a PV-cre mouse (Fig. 4B), we identified one network that was limited to two neurons, with a δL of 9.0% and intersomatic distance of 43.5 µm.

Discussion

Electrical synapses are widely expressed throughout the adult mammalian brain, yet functional measurements and maps of their networks remain entirely absent in live tissue. Here we introduce opto-δL, which leverages focal photostimulation of opsin-expressing neurons combined with measurements of changes in spike timing, including tests of significance, resulting from excitation across electrical synapses. Using opto-δL, we show that GABAergic TRN neurons of differing molecular subtypes are coupled in homocellular and heterocellular electrical networks and extend further across tissue than previously identified by dual-cell patching[73]. Further, we identify functional network size, which is limited to far fewer neurons than dye coupling had previously suggested[62].

In our experiments in TRN, we observed PV neurons without electrical synapses less frequently than among SOM neurons (Fig. 3B). We hypothesize that reflects that PV expression is more of an umbrella than a distinct marker for a subset of TRN neurons, as has long been believed[52, 53, 78-82], and therefore, our maps of PV neurons might include both heterocellular and homocellular electrical synapses. However, other experiments suggest that PV neurons are a

226 distinct subset of TRN neurons that primarily form connections with first-order thalamus[51, 83],
227 similar to subsets identified by the protein CB[53] and the transcription factor SPP1[52], and distinct
228 from SOM+ neurons. If the latter were the case, our results imply that TRN neurons that project
229 to first-order thalamus form more electrical synapses than SOM neurons. In turn, that difference
230 would imply that coordination between larger numbers of TRN neurons is more prevalent for
231 first-order thalamus.

232 The electrical connections we observed in networks emanating from one neuron were small,
233 ranging from 1 to 4 electrical synapses; these are the first measurements of the number of direct
234 electrical synapses composing a network. A previous dye-coupling study in juvenile TRN stained
235 networks with an average of 7 neurons, and as large as 10 to 20 neurons[62]. Dye-coupling allows
236 spread between neurons that are not directly coupled to the originally patched neuron, but it is
237 unlikely that an indirectly coupled neuron would affect spike timing by the magnitudes we
238 regularly observed. Our observations of networks of 1-4 neurons are consistent with results
239 inferring that TRN neurons form small clusters of coupled neurons[73].

240 As is the case with all focal optogenetic stimuli, opto-δL must account for the effects of off-
241 target stimulation due to photons scattering in tissue. Previous work measuring chemical
242 postsynaptic responses used post-hoc filtering of direct photostimulation artifacts, leveraging
243 distinctions in channel and photocurrent kinetics[76, 84]. Opto-δL accounts for the problem of light
244 scatter by comparing shifts in spike latencies caused by photostimulating a neuron to spike
245 latencies when an equidistant location is photostimulated (Fig. 1, Supp Fig. 3, see methods).

246 Opto-δL can be implemented in other brain regions, as shown by the network maps we
247 created in cortex (Figure 4). Unlike TRN, cortex is a mix of inhibitory and excitatory neurons,
248 and potentially coupled inhibitory neurons may be separated by longer distances. In cortex, an

249 additional barrier to identifying and measuring coupling by paired patching is the need to
250 visually identify GABAergic neurons. Use of fluorescent labels in opto-δL mitigates this barrier,
251 although it remains for targeting heterocellular networks.

252 Our experiments likely undersampled electrical synapses and networks for several reasons.
253 First, slicing brain tissue cuts some connections, causing some neuron loss. Second, our previous
254 experiments determined that heterocellular synapses are common[54], but we were unable to
255 photostimulate neurons that did not express opsin, which represent another pool of possibly
256 undetected coupling. Failure of virus transfection for some neurons could be a source of
257 misidentification in our experiments. Furthermore, due to experimental time constraints, we only
258 tested a subset of nearby neurons for each patched neuron; it is possible that we missed some
259 untested connections in experiments. Our method may also underestimate connections due to a
260 floor effect from light scatter compensation and differences in sensitivity between cc and δL to
261 very weak synapses. Therefore, while our experiments failed to detect any electrical synapses for
262 26 neurons, we expect that we overestimated the number of TRN neurons without electrical
263 synapses. It is possible that a subset of TRN neurons exists without electrical synapses, which
264 would be consistent with the observation that some TRN neurons do not stain for Cx36[56].
265 Likewise, we interpret our report of 1 to 4 electrical synapses for TRN networks as establishing a
266 floor for electrical network size.

267 Measurements of δL can in principle be used *in vivo* with focal holographic stimulation to
268 map electrical synapses, and we suggest that this would be a valuable next step to establish more
269 accurate TRN networks fully in three dimensions. As a tool, opto-δL opens the possibility for
270 more easily detecting and measuring coupled networks throughout the brain. For example, one
271 could examine how a network changes in response to different plasticity paradigms.

Alternatively, combining opto-δL with calcium imaging can be informative as to how members of a network respond to different inputs.

Methods

Animals

SOM-Cre (Jax: 028532) or PV-Cre (Jax: 013044) mice were used for experiments. Mice were at least P28 for surgeries and P42 for electrophysiological recordings. For one juvenile experiment (Fig. 1), a calbindin-Cre (Jax: 028532) mouse was injected at P0 and electrophysiological recordings occurred at P14.

Electrophysiology

Mice were transcardially perfused with NMDG ACSF solution (in mM): 92 NMDG, 2.5 KCl, 1.25 NaH_2PO_4, 30 $NAHCO_3$, 20 HEPES, 25 glucose, 2 thiourea, 5 NA ascorbate, 3 NA pyruvate, 0.5 $CaCl_2$, and 10 $MgSO_4 \cdot 7H_2O$ (315 mOsm L^{-1}, 7.3-7.4 pH). Horizontal brain slices 250 µm thick were cut and incubated in NMDG solution. Slices were incubated at 34°C for 12-15 min in NMDG following cutting and returned to HEPES ACSF at room temperature until recording. The HEPES ACSF solution comprised in mM: 92 NaCl, 2.5 KCl, 1.25 NaH_2PO_4, 30 $NaHCO_3$, 20 HEPES, 25 glucose, 2 Thiourea, Na ascorbate, NA pyruvate, 2 CaCl2, and 2 $MgSO_4 \cdot 7H_20$ (315 mOsm L^{-1}, 7.3-7.4 pH). The ACSF bath during recording contained (in mM): 126 NaCl, 3 KCl, 1.25 NaH_2PO_4, 2 $MgSO_4$, 26 $NaHCO_3$, 10 dextrose, and 2 $CaCl_2$ (315–320 mOsm L^{-1}, saturated with 95% O_2/5% CO_2). The submersion recording chamber was held at 34°C (TC-324B, Warner Instruments). Electrodes were filled with (in mM): 135 potassium gluconate, 2 KCl, 4 NaCl, 10 Hepes, 0.2 EGTA, 4 ATP-Mg, 0.3 GTP-Tris, and 10 phosphocreatine-Tris (pH 7.25, 295 mOsm L^{-1}). 1 M KOH was used to adjust pH of the internal

294 solution. The approximate bath flowrate was 2 ml min^{-1} and the recording chamber held
295 approximately 5 ml solution.

296 The TRN was visualized under 4x magnification, and pairs of adjacent TRN cells from any
297 sensory sector were identified and patched under 40x IR-DIC optics (SliceScope, Scientifica,
298 Uckfield, UK). Cell type was determined by mRuby epifluorescence in the patched neurons.
299 Cells with low fluorescent contrast were avoided. The mRuby reporter was excited by a 560 nm
300 diode delivered through the objective (CoolLED pE-300). Voltage signals were amplified and
301 lowpass filtered at 8 kHz (MultiClamp, Axon Instruments, Molecular Devices, Sunnyvale, CA,
302 USA), digitized at 20 kHz with custom Matlab routines controlling a National Instruments
303 (Austin, TX, USA, USB6221 DAQ board), and data were stored for offline analysis in Matlab
304 (Mathworks, R2023b, Natick, MA, USA). Recordings were made in whole-cell current-clamp
305 mode. Negative current was used to maintain cells at −70 mV to -60 mV during recordings.
306 Pipette resistances were 5 - 9 MΩ before bridge balance; recordings were discarded if access
307 resistance exceeded 25 MΩ. Voltages are reported uncorrected for the liquid junction potential.

308 *Stereotaxic surgery*

309 SOM-Cre (Jax: 028532) or PV-Cre (Jax: 013044) mice were anesthetized via inhaled
310 isoflurane (0.8-1.2%) and 0.1 mL of 0.015 mg/mL buprenorphine via intraparietal injection.
311 Mice were positioned on a heated pad and in a stereotax (Kopf). After exposure of the skull, a
312 dental drill was used to open a hole above the injection site. Then, AAV9-CAG-DIO-ChroME-st-
313 P2A-H2B-mRuby (titer 2.7 x 10^{13} GC/mL) was injected at a rate of 100 nL/min (WPI UMP-3).
314 The coordinates for injection were -1.35 AP, ± 2.1 ML, -3.0 and -3.2 DV for TRN and -0.5 AP, ±
315 3.0 ML, -2.0 and -2.6 DV for somatosensory cortex. We injected a total of 600 nL of virus for
316 TRN and 800 nL of virus for somatosensory cortex. Post surgery and scalp suturing, mice were

317 given an intraperitoneal injection of 0.1 mL of 0.5 mg/mL carprofen and 1 mL saline, and
318 monitored for recovery. Mice were given at least two weeks for viral expression before
319 experiments. For the juvenile surgery, a calbindin-Cre (Jax: 028532) mouse was anesthetized via
320 hypothermia on a cold metal plate, and the coordinates for injection targeting TRN were -1.4 AP,
321 ± 1.9 ML, -1.4 and -1.9 DV.

322 *Image processing*

323 *All fluorescent images were modified in Fiji and psuedocolored to facilitate visualization.*

324 *Optogenetic δL*

325 For the rheobase current necessary to measure δL, we used the smallest stimuli that drove
326 spiking at least 80% of the time. Trials were excluded if latency to spike was less than 20 ms
327 when the neuron was given a rheobase stimulus.

328 To perform single-cell optogenetic stimulation, we used a 560 nm LED (Mightex) and
329 digital mirror device (Mightex Polygon 1000) to direct light to an area the size of an individual
330 soma (7 - 8 µm diameter circle). The area size used mostly covered the entire soma without
331 extending beyond the edge of the soma. Prior to any experiments, we patched an opsin-
332 expressing cell to determine an intensity of light that was sufficient to drive bursts for a 50 ms
333 stimulus, and then used a photostimulus that was 50% stronger for all subsequent experiments in
334 that slice. Light intensity ranged from 3.7 - 99.8 mW/mm^2 with most experiments occurring in
335 6.2 - 25.0 mW/mm^2 range.

336 Single-cell optogenetic stimulation is confounded by off-target excitation by light scatter for
337 both 1 photon and 2 photon stimulation paradigms[74-76]. For the purposes of mapping synaptic
338 connections, scatter-induced photostimulation of the patched neuron is a potential confound.

339 Depolarization from photostimulation caused by light scatter is directly proportional to the
340 distance between the patched neuron and focal stimulation (Supp. Fig. 2). Opto-δL is well-suited
341 to overcome the problem of unintended photostimulation to the patched neuron because the
342 method quantifies latency of spikes rather than voltage changes. Consequently, comparing
343 latency of spikes when a nearby neuron is photostimulated to latency when an equidistant empty
344 control location is photostimulated allowed us to distinguish the contribution of GJs to spike
345 times.

346 After patching TRN neurons from any sensory sector, we used one of two methods to first
347 make measurements that would control for the effects of light scattering, and then to compute
348 δL.

349 i) Corrections to δL: We delivered a rheobase stimulus to the patched neuron alone 10
350 times. Interleaved between those stimulations, we gave the neuron a rheobase
351 stimulus while also focally photostimulating either a nearby mRuby+ neuron or an
352 equidistant empty spot. Offline, we measured the latency of spikes from stimulation
353 onset for each condition. We report δL as the change in latency induced by focal
354 photostimulation of the nearby neuron minus the change in latency induced by
355 photostimulation of an empty area.
356

357 ii) Correction to Iapp: We applied focal photostimulation ten times to an empty location
358 equidistant from the patched neuron as the nearby neuron of interest. We measured
359 the average depolarizing current that resulted from the light scattering. We then
360 adjusted rheobase Iapp by average current caused by light scatter (Supp. Fig. 3) and
361 used that adjusted Iapp while photostimulating the nearby mRuby+ or an equidistant

empty location. Offline, we calculated δL by comparing latency changes between when light targeted the empty control location (t1) compared to light targeting the mRuby+ neuron (t1).

We used corrected δL directly for 30 homocellular network measurements, and we used correction to I_{app} for 29 homocellular network measurements.

Numerical analysis

To calculate δL we used the average spike latency from control trials (t_1) and average spike latency when a nearby neuron was photostimulated (t_2):

$$\delta L = \frac{100 * (t_1 - t_2)}{t_1}$$

We tested δLs for significance with a Wilcoxon signed-rank test. We compared δLs between different neuronal subtypes via Mann-Whitney U test, and we used Chi-squared tests to compare electrical synapses counts per network between different genetic subtypes. Statistical tests were considered significant when $p < 0.05$. In our analysis of network size, we only included experiments where three or more possible connections were tested.

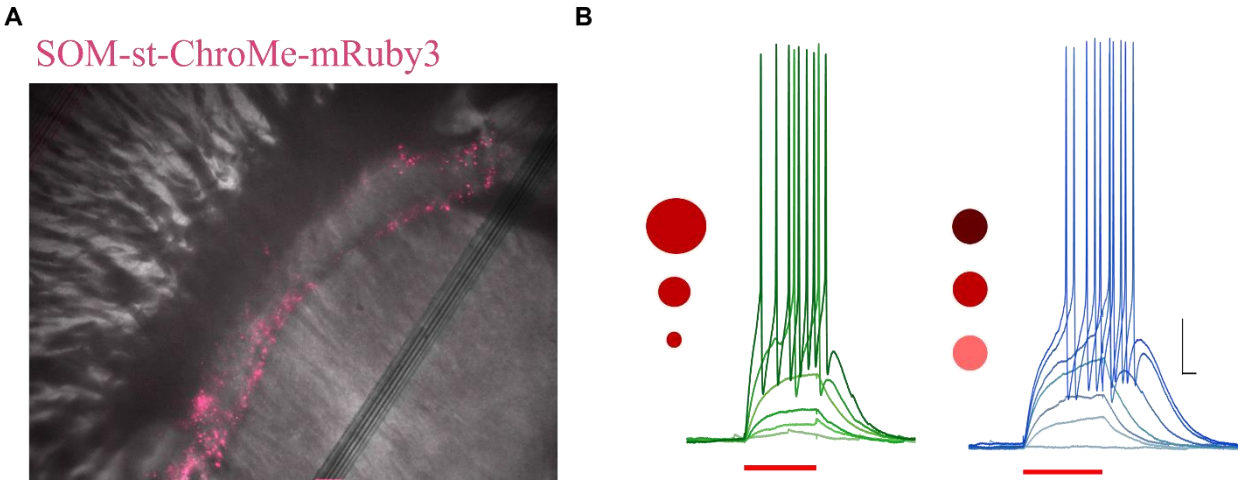

Supplementary Figure 1: Validation of single-cell focal photostimulation. A. Expression pattern of st-ChoME-mRuby3 via AAV injection in a SOM-Cre mouse (fluorescence pseudocolored magenta). Expression was restricted to the shell of TRN. **B.** Left, spiking driven by increasing area of light in a spot (3.14, 7.07, 14.14, 22.0, 31.4, 47.2 μm^2 circles). Right, spiking driven by increasing light intensity (24.4, 37.1, 59.2, 66.2, 80.1, 87.0, 105.7 mW/mm^2). Scale bar 25 ms, 10 mV. V_m = -61 mV.

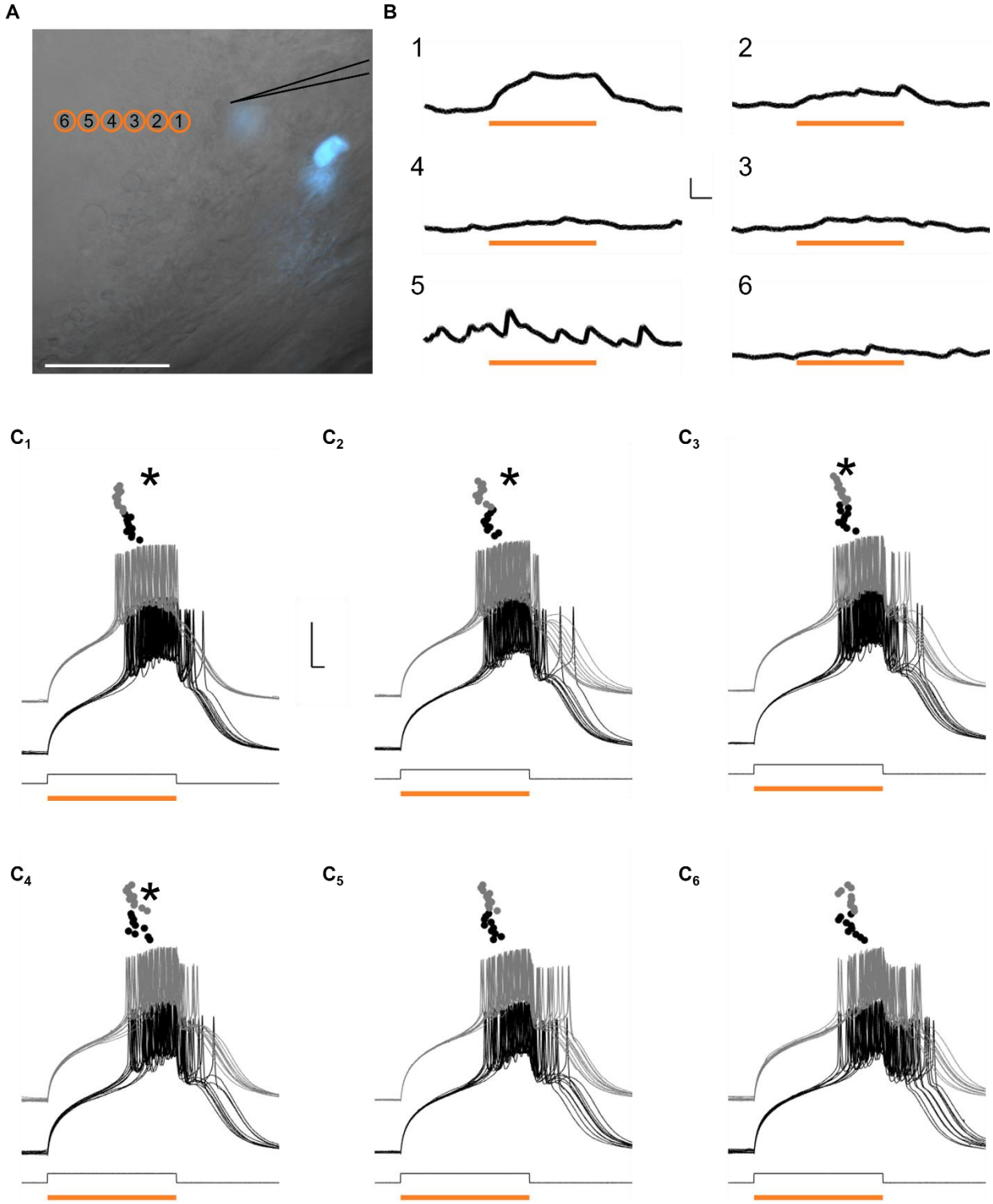
A
6 5 4 3 2 1
B
1
2
4
3
5
6
C1
C2
C3
C4
C5
C6
*

Supplementary Figure 2: **Example of excitation from light scattering. A.** Overlay of IR and fluorescence images from live recording of st-ChroME-mRuby-expressing neurons in PV-Cre mouse. Empty locations were serially photostimulated by increasing 10 µm intervals measured from the edge of the soma from the patched neuron. The power of the photostimulation was 10.5 mW/mm^2 and was sufficient to drive the neuron to burst when targeted on the soma. Scale bar: 50 µm. **B.** Voltage responses of the patched neuron from focally stimulating the corresponding numbered locations in A. Scale bar: 10 ms, 1 mV. **C.** Shifts in in spike latency caused by focally photostimulating empty locations in A. **C1.** $\delta L = 13.4\%$, $p < 0.01$. **C2.** $\delta L = 9.2\%$, $p < 0.01$. **C3.** $\delta L = 5.2\%$, $p < 0.01$. **C4.** $\delta L = 3.9\%$, $p = 0.04$. **C5.** $\delta L = 3.5\%$, $p = 0.07$. **C6.** $\delta L = 1.8\%$, $p = 0.38$. Scale bar: 5 ms, 20 mV. Asterix mark significance ($p < 0.05$, Wilcoxon signed-rank test).

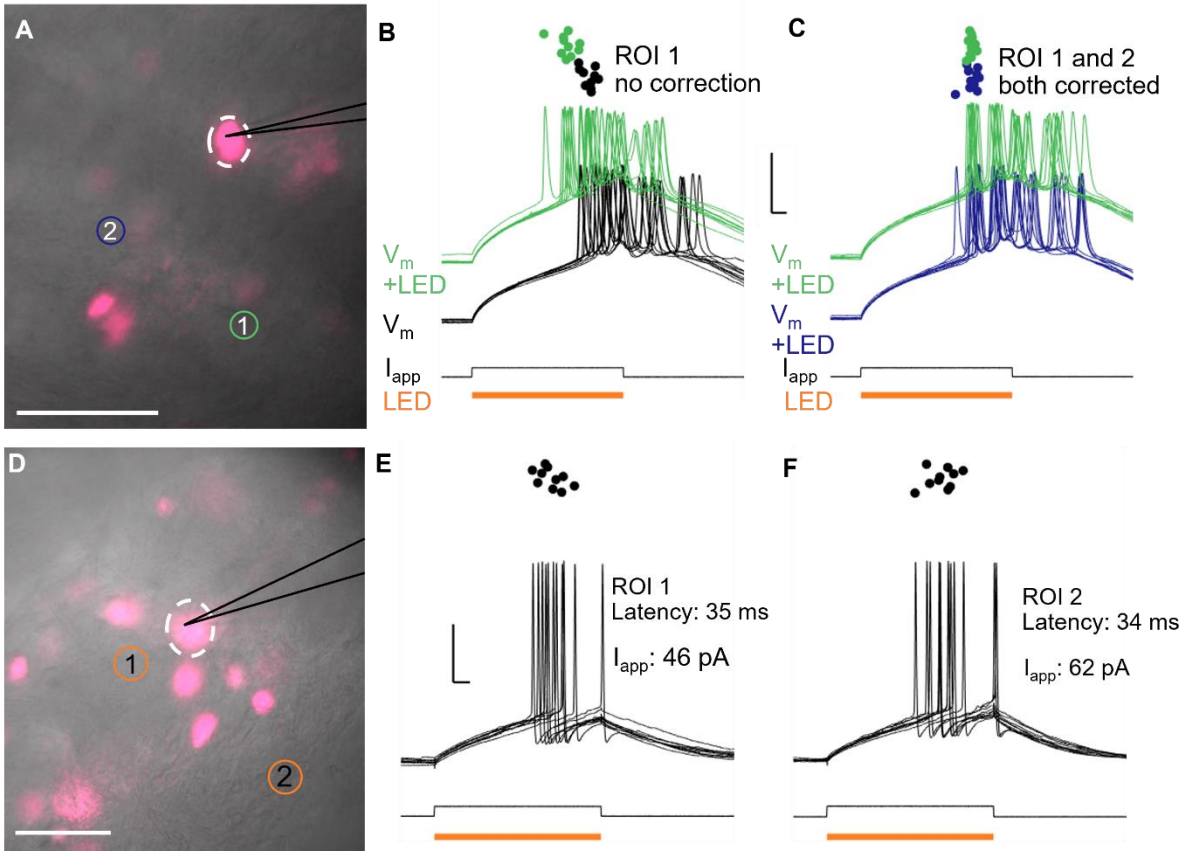

Supplementary Figure 3: **Compensation for effects of scatter-induced photoexcitation on spike times.** **A.** Overlay of IR and fluorescent images of ChroME-mRuby-expressing neurons in a SOM-Cre mouse. Fluorescence is pseudocolored magenta. Scale bar: 50 µm. The patched neuron is circled with white dashes. Empty regions of interests (ROIs) (e.g. orange circles) at different distances were photostimulated to determine the compensation for scatter to rheobase for the patched neuron. **B.** Spiking responses for rheobase (51 pA) applied current alone (black traces; mean latency 38.6 ms) or during simultaneous photostimulation of ROI1 (green traces, mean latency 31.2 ms). Dots mark the times of first spikes from each trial. Uncompensated scatter from ROI 1 caused a false δL of 19%. **C.** Spiking responses for compensated rheobase (22 pA) and simultaneous photostimulation of ROI 2 (blue traces; mean latency 36.6 ms), and for compensated rheobase during photostimulation of ROI 1 (green traces; mean latency 36.5 ms). **D**. Overlay of IR and fluorescence (pseudocolor: magenta) images of ChroME-mRuby-expressing neurons in a slice from a SOM-Cre mouse. Scale bar 50 µm. The patched neuron is circled with white dashes. Without any photostimuli, rheobase was determined to be 65 pA. Two non-fluorescing ROIs, circled in orange, were selected for photostimulation. **E.** Spiking in the recorded neuron after correction of rheobase (square pulse, lower) for scatter to 46 pA during photostimulation of ROI 1 (orange bar). The corrected mean latency of the first spike was 35 ms. **F.** Spiking in the recorded neuron after correction of rheobase for scatter to 62 pA (square pulse, below) during photostimulation of ROI 2 (red bar). The mean corrected latency of the first spike was 34 ms. Scale bars are 25 ms, 10 mV.

1. Belluardo N, Mudò G, Trovato-Salinaro A, Le Gurun S, Charollais A, Serre-Beinier V, Amato G, Haefliger J-A, Meda P, Condorelli DF. Expression of connexin36 in the adult and developing rat brain. Brain research. 2000;865(1):121-38.
2. Condorelli DF, Belluardo N, Trovato-Salinaro A, Mudò G. Expression of Cx36 in mammalian neurons. Brain Research Reviews. 2000;32(1):72-85.

3. Rash J, Staines W, Yasumura T, Patel D, Furman C, Stelmack G, Nagy J. Immunogold evidence that neuronal gap junctions in adult rat brain and spinal cord contain connexin-36 but not connexin-32 or connexin-43. Proceedings of the National Academy of Sciences. 2000;97(13):7573-8.
4. Bennett MV, Zukin RS. Electrical coupling and neuronal synchronization in the Mammalian brain. Neuron. 2004;41(4):495-511. Epub 2004/02/26. doi: 10.1016/s0896-6273(04)00043-1. PubMed PMID: 14980200.
5. Abbott L, Marder E, Hooper SL. Oscillating networks: control of burst duration by electrically coupled neurons. Neural Computation. 1991;3(4):487-97.
6. Traub RD, Kopell N, Bibbig A, Buhl EH, LeBeau FE, Whittington MA. Gap junctions between interneuron dendrites can enhance synchrony of gamma oscillations in distributed networks. Journal of Neuroscience. 2001;21(23):9478-86.
7. Gutierrez GJ, O'Leary T, Marder E. Multiple mechanisms switch an electrically coupled, synaptically inhibited neuron between competing rhythmic oscillators. Neuron. 2013;77(5):845-58.
8. Destexhe A. Spike-and-wave oscillations based on the properties of GABAB receptors. Journal of Neuroscience. 1998;18(21):9099-111.
9. Draguhn A, Traub R, Schmitz D, Jefferys J. Electrical coupling underlies high-frequency oscillations in the hippocampus in vitro. Nature. 1998;394(6689):189-92.
10. Whittington MA, Traub RD. Interneuron diversity series: inhibitory interneurons and network oscillations in vitro. Trends in neurosciences. 2003;26(12):676-82.
11. Chow CC, Kopell N. Dynamics of spiking neurons with electrical coupling. Neural Comput. 2000;12(7):1643-78. Epub 2000/08/10. doi: 10.1162/089976600300015295. PubMed PMID: 10935921.
12. Haas JS, Landisman CE. State-dependent modulation of gap junction signaling by the persistent sodium current. Front Cell Neurosci. 2011;5:31. Epub 2012/02/10. doi: 10.3389/fncel.2011.00031. PubMed PMID: 22319469; PMCID: PMC3263475.
13. Pernelle G, Nicola W, Clopath C. Gap junction plasticity as a mechanism to regulate network-wide oscillations. PLoS computational biology. 2018;14(3):e1006025.
14. Pfeuty B, Mato G, Golomb D, Hansel D. The combined effects of inhibitory and electrical synapses in synchrony. Neural Computation. 2005;17(3):633-70.
15. Pfeuty B, Mato G, Golomb D, Hansel D. Electrical synapses and synchrony: the role of intrinsic currents. Journal of Neuroscience. 2003;23(15):6280-94.
16. DeVries SH, Qi X, Smith R, Makous W, Sterling P. Electrical coupling between mammalian cones. Current Biology. 2002;12(22):1900-7.
17. Medvedev GS. Electrical coupling promotes fidelity of responses in the networks of model neurons. Neural computation. 2009;21(11):3057-78.
18. Zhu P, Frank T, Friedrich RW. Equalization of odor representations by a network of electrically coupled inhibitory interneurons. Nature neuroscience. 2013;16(11):1678-86.
19. Galarreta M, Hestrin S. Spike transmission and synchrony detection in networks of GABAergic interneurons. Science. 2001;292(5525):2295-9.
20. Gibson JR, Beierlein M, Connors BW. Functional properties of electrical synapses between inhibitory interneurons of neocortical layer 4. Journal of neurophysiology. 2005;93(1):467-80.
21. Russo G, Nieus TR, Maggi S, Taverna S. Dynamics of action potential firing in electrically connected striatal fast-spiking interneurons. Frontiers in cellular neuroscience. 2013;7:209.
22. Apostolides PF, Trussell LO. Control of interneuron firing by subthreshold synaptic potentials in principal cells of the dorsal cochlear nucleus. Neuron. 2014;83(2):324-30.

23. Trenholm S, McLaughlin AJ, Schwab DJ, Awatramani GB. Dynamic tuning of electrical and chemical synaptic transmission in a network of motion coding retinal neurons. Journal of Neuroscience. 2013;33(37):14927-38.
24. Deans MR, Volgyi B, Goodenough DA, Bloomfield SA, Paul DL. Connexin36 is essential for transmission of rod-mediated visual signals in the mammalian retina. Neuron. 2002;36(4):703-12.
25. Christie JM, Westbrook GL. Lateral excitation within the olfactory bulb. Journal of Neuroscience. 2006;26(8):2269-77.
26. Ren Y, Liu Y, Luo M. Gap Junctions Between Striatal D1 Neurons and Cholinergic Interneurons. Frontiers in Cellular Neuroscience. 2021;15:191.
27. Veruki ML, Hartveit E. Electrical synapses mediate signal transmission in the rod pathway of the mammalian retina. Journal of Neuroscience. 2002;22(24):10558-66.
28. Alcami P. Electrical synapses enhance and accelerate interneuron recruitment in response to coincident and sequential excitation. Frontiers in cellular neuroscience. 2018;12:156.
29. Rabinowitch I, Chatzigeorgiou M, Schafer WR. A gap junction circuit enhances processing of coincident mechanosensory inputs. Current Biology. 2013;23(11):963-7.
30. Pham T, Haas JS. Electrical synapses regulate both subthreshold integration and population activity of principal cells in response to transient inputs within canonical feedforward circuits. PLoS computational biology. 2019;15(2):e1006440.
31. Pham T, Haas JS. Electrical synapses between inhibitory neurons shape the responses of principal neurons to transient inputs in the thalamus: a modeling study. Scientific reports. 2018;8(1):1-12.
32. Hoehne A, McFadden MH, DiGregorio DA. Feed-forward recruitment of electrical synapses enhances synchronous spiking in the mouse cerebellar cortex. Elife. 2020;9:e57344.
33. Kuo SP, Schwartz GW, Rieke F. Nonlinear spatiotemporal integration by electrical and chemical synapses in the retina. Neuron. 2016;90(2):320-32.
34. Szarka G, Ganczer A, Balogh M, Tengölics ÁJ, Futácsi A, Kenyon G, Pan F, Kovács-Öller T, Völgyi B. Gap Junctions Fine-tune Ganglion Cell Signals to Equalize Response Kinetics within a Given Electrically Coupled Array. iScience. 2024.
35. Cooler S, Schwartz GW. An offset ON–OFF receptive field is created by gap junctions between distinct types of retinal ganglion cells. Nature neuroscience. 2021;24(1):105-15.
36. Wang S, Borst A, Zaslavsky N, Tishby N, Segev I. Efficient encoding of motion is mediated by gap junctions in the fly visual system. PLoS computational biology. 2017;13(12):e1005846.
37. Bennett MV. Physiology of electrotonic junctions. Ann N Y Acad Sci. 1966;137(2):509-39. Epub 1966/07/14. doi: 10.1111/j.1749-6632.1966.tb50178.x. PubMed PMID: 5229812.
38. van Welie I, Roth A, Ho SS, Komai S, Häusser M. Conditional spike transmission mediated by electrical coupling ensures millisecond precision-correlated activity among interneurons in vivo. Neuron. 2016;90(4):810-23.
39. Stewart WW. Functional connections between cells as revealed by dye-coupling with a highly fluorescent naphthalimide tracer. Cell. 1978;14(3):741-59.
40. Connors B, Benardo L, Prince D. Coupling between neurons of the developing rat neocortex. Journal of Neuroscience. 1983;3(4):773-82.
41. Hampson EC, Weiler R, Vaney DI. pH-gated dopaminergic modulation of horizontal cell gap junctions in mammalian retina. Proc Biol Sci. 1994;255(1342):67-72. Epub 1994/01/22. doi: 10.1098/rspb.1994.0010. PubMed PMID: 8153138.
42. Hampson E, Vaney DI, Weiler R. Dopaminergic modulation of gap junction permeability between amacrine cells in mammalian retina. Journal of Neuroscience. 1992;12(12):4911-22.
43. Peinado A, Yuste R, Katz LC. Extensive dye coupling between rat neocortical neurons during the period of circuit formation. Neuron. 1993;10(1):103-14.

44. Onn S, Grace AA. Dye coupling between rat striatal neurons recorded in vivo: compartmental organization and modulation by dopamine. Journal of Neurophysiology. 1994;71(5):1917-34.
45. Mills SL, Xia XB, Hoshi H, Firth SI, Rice ME, Frishman LJ, Marshak DW. Dopaminergic modulation of tracer coupling in a ganglion-amacrine cell network. Vis Neurosci. 2007;24(4):593-608. Epub 2007/08/23. doi: 10.1017/S0952523807070575. PubMed PMID: 17711603; PMCID: PMC2213423.
46. Ribelayga C, Cao Y, Mangel SC. The circadian clock in the retina controls rod-cone coupling. Neuron. 2008;59(5):790-801. Epub 2008/09/13. doi: 10.1016/j.neuron.2008.07.017. PubMed PMID: 18786362; PMCID: PMC5581203.
47. Qiao M, Sanes JR. Genetic method for labeling electrically coupled cells: application to retina. Frontiers in molecular neuroscience. 2016;8:81.
48. Tian L, Yang Y, Wysocki LM, Arnold AC, Hu A, Ravichandran B, Sternson SM, Looger LL, Lavis LD. Selective esterase–ester pair for targeting small molecules with cellular specificity. Proceedings of the National Academy of Sciences. 2012;109(13):4756-61.
49. Pinault D. The thalamic reticular nucleus: structure, function and concept. Brain Res Brain Res Rev. 2004;46(1):1-31. Epub 2004/08/07. doi: 10.1016/j.brainresrev.2004.04.008. PubMed PMID: 15297152.
50. Crick F. Function of the thalamic reticular complex: the searchlight hypothesis. Proc Natl Acad Sci U S A. 1984;81(14):4586-90. Epub 1984/07/01. doi: 10.1073/pnas.81.14.4586. PubMed PMID: 6589612; PMCID: PMC345636.
51. Clemente-Perez A, Makinson SR, Higashikubo B, Brovarney S, Cho FS, Urry A, Holden SS, Wimer M, Dávid C, Fenno LE. Distinct thalamic reticular cell types differentially modulate normal and pathological cortical rhythms. Cell reports. 2017;19(10):2130-42.
52. Li Y, Lopez-Huerta VG, Adiconis X, Levandowski K, Choi S, Simmons SK, Arias-Garcia MA, Guo B, Yao AY, Blosser TR. Distinct subnetworks of the thalamic reticular nucleus. Nature. 2020:1-6.
53. Martinez-Garcia RI, Voelcker B, Zaltsman JB, Patrick SL, Stevens TR, Connors BW, Cruikshank SJ. Two dynamically distinct circuits drive inhibition in the sensory thalamus. Nature. 2020;583(7818):813-8.
54. Vaughn MJ, Laswick Z, Wang H, Haas JS. Functionally distinct circuits are linked by heterocellular electrical synapses in the thalamic reticular nucleus. eneuro. 2023;11(1).
55. Hartley ND, Krol A, Choi S, Rome N, Levandowski K, Pasqualoni S, Jones C, Tian J, Lee S, Lee H. Distinct structural and functional connectivity of genetically segregated thalamoreticular subnetworks. Cell Reports. 2024;43(12).
56. Landisman CE, Long MA, Beierlein M, Deans MR, Paul DL, Connors BW. Electrical synapses in the thalamic reticular nucleus. J Neurosci. 2002;22(3):1002-9. Epub 2002/02/05. PubMed PMID: 11826128; PMCID: PMC6758490.
57. Haas JS, Zavala B, Landisman CE. Activity-dependent long-term depression of electrical synapses. Science. 2011;334(6054):389-93. Epub 2011/10/25. doi: 10.1126/science.1207502. PubMed PMID: 22021860.
58. Sevetson J, Haas JS. Asymmetry and modulation of spike timing in electrically coupled neurons. J Neurophysiol. 2015;113(6):1743-51. Epub 2014/12/30. doi: 10.1152/jn.00843.2014. PubMed PMID: 25540226.
59. Landisman CE, Connors BW. Long-term modulation of electrical synapses in the mammalian thalamus. Science. 2005;310(5755):1809-13.

60. Deleuze C, Huguenard JR. Distinct electrical and chemical connectivity maps in the thalamic reticular nucleus: potential roles in synchronization and sensation. Journal of Neuroscience. 2006;26(33):8633-45.
61. Lam Y-W, Nelson CS, Sherman SM. Mapping of the functional interconnections between thalamic reticular neurons using photostimulation. Journal of neurophysiology. 2006;96(5):2593-600.
62. Lee S-C, Patrick SL, Richardson KA, Connors BW. Two functionally distinct networks of gap junction-coupled inhibitory neurons in the thalamic reticular nucleus. Journal of Neuroscience. 2014;34(39):13170-82.
63. Degen J, Meier C, Van Der Giessen RS, Söhl G, Petrasch-Parwez E, Urschel S, Dermietzel R, Schilling K, De Zeeuw CI, Willecke K. Expression pattern of lacZ reporter gene representing connexin36 in transgenic mice. Journal of Comparative Neurology. 2004;473(4):511-25.
64. Blethyn KL, Hughes SW, Crunelli V. Evidence for electrical synapses between neurons of the nucleus reticularis thalami in the adult brain in vitro. Thalamus & related systems. 2008;4(1):13-20.
65. Mainen ZF, Sejnowski TJ. Reliability of spike timing in neocortical neurons. Science. 1995;268(5216):1503-6.
66. Gütig R. To spike, or when to spike? Current opinion in neurobiology. 2014;25:134-9.
67. VanRullen R, Guyonneau R, Thorpe SJ. Spike times make sense. Trends in neurosciences. 2005;28(1):1-4.
68. Stüttgen MC, Schwarz C. Psychophysical and neurometric detection performance under stimulus uncertainty. Nature neuroscience. 2008;11(9):1091-9.
69. Gollisch T, Meister M. Rapid neural coding in the retina with relative spike latencies. science. 2008;319(5866):1108-11.
70. Kilinc D, Demir A. Spike timing precision of neuronal circuits. Journal of computational neuroscience. 2018;44:341-62.
71. Haas JS. A new measure for the strength of electrical synapses. Frontiers in cellular neuroscience. 2015;9:378.
72. Mardinly AR, Oldenburg IA, Pégard NC, Sridharan S, Lyall EH, Chesnov K, Brohawn SG, Waller L, Adesnik H. Precise multimodal optical control of neural ensemble activity. Nature neuroscience. 2018;21(6):881-93.
73. Long MA, Landisman CE, Connors BW. Small clusters of electrically coupled neurons generate synchronous rhythms in the thalamic reticular nucleus. Journal of Neuroscience. 2004;24(2):341-9.
74. Shemesh OA, Tanese D, Zampini V, Linghu C, Piatkevich K, Ronzitti E, Papagiakoumou E, Boyden ES, Emiliani V. Temporally precise single-cell-resolution optogenetics. Nature neuroscience. 2017;20(12):1796-806.
75. Hage TA, Bosma-Moody A, Baker CA, Kratz MB, Campagnola L, Jarsky T, Zeng H, Murphy GJ. Synaptic connectivity to L2/3 of primary visual cortex measured by two-photon optogenetic stimulation. Elife. 2022;11:e71103.
76. Antin B, Sadahiro M, Gajowa M, Triplett MA, Adesnik H, Paninski L. Removing direct photocurrent artifacts in optogenetic connectivity mapping data via constrained matrix factorization. PLOS Computational Biology. 2024;20(5):e1012053.
77. Hu H, Cavendish JZ, Agmon A. Not all that glitters is gold: off-target recombination in the somatostatin–IRES-Cre mouse line labels a subset of fast-spiking interneurons. Frontiers Media SA; 2013. p. 195.
78. Frassoni C, Bentivoglio M, Spreafico R, Sánchez MP, Puelles L, Fairen A. Postnatal development of calbindin and parvalbumin immunoreactivity in the thalamus of the rat. Developmental brain research. 1991;58(2):243-9.

79. Mitrofanis J. Patterns of antigenic expression in the thalamic reticular nucleus of developing rats. Journal of Comparative Neurology. 1992;320(2):161-81.
80. Hou G, Smith AG, Zhang ZW. Lack of Intrinsic GABAergic Connections in the Thalamic Reticular Nucleus of the Mouse. J Neurosci. 2016;36(27):7246-52. Epub 2016/07/08. doi: 10.1523/JNEUROSCI.0607-16.2016. PubMed PMID: 27383598; PMCID: PMC4938865.
81. Thankachan S, Katsuki F, McKenna JT, Yang C, Shukla C, Deisseroth K, Uygun DS, Strecker RE, Brown RE, McNally JM. Thalamic reticular nucleus parvalbumin neurons regulate sleep spindles and electrophysiological aspects of schizophrenia in mice. Scientific reports. 2019;9(1):1-16.
82. Seto-Ohshima A, Emson P, Berchtold M, Heizmann C. Localization of parvalbumin mRNA in rat brain by in situ hybridization histochemistry. Experimental brain research. 1989;75(3):653-8.
83. Hoseini MS, Higashikubo B, Cho FS, Chang AH, Clemente-Perez A, Lew I, Ciesielska A, Stryker MP, Paz JT. Gamma rhythms and visual information in mouse V1 specifically modulated by somatostatin+ neurons in reticular thalamus. Elife. 2021;10:e61437.
84. Printz Y, Patil P, Mahn M, Benjamin A, Litvin A, Levy R, Bringmann M, Yizhar O. Determinants of functional synaptic connectivity among amygdala-projecting prefrontal cortical neurons in male mice. Nature communications. 2023;14(1):1667.